Geophys. J. R. astr. Soc. (1986) **86**, 863–883

An instability theory of ice–air interaction for the migration of the marginal ice zone

P. C. Chu *Department of Geophysical Sciences, The University of Chicago, Chicago, IL 60637, USA*

Accepted 1986 February 28. Received 1986 February 14; in original form 1985 June 10

Summary. A guided discharge of ice into the belt of subpolar and midlatitude westerlies from the polar region is observed near the east side of both the Antarctic Peninsula and Greenland. Meteorological observations (Schwerdtfeger) show that moderate to strong southerly surface winds often develop along the marginal ice zone (MIZ) near the east side of the Antarctic Peninsula. Such strong winds are generated by surface temperature gradient over ice and water. These surface winds, acting through stress, in turn force the drift of the MIZ. This implies an ice–air feedback mechanism. A coupled air–ice model is established to discuss the instability properties of such a feedback mechanism. The model consists of two parts: thermally forced boundary layer air flow (Kuo) and mechanically forced MIZ drift. The two components are linked through surface temperature gradient and surface wind stress. The coupled ice–air model is solved for different values of the three parameters: (a) mean ice thickness H_i (0.5 m $< H_i <$ 10.5 m), (b) mean surface temperature difference over ice and water DT_0 (1°C $< DT_0 <$ 21°C), and (c) Brunt–Väisälä frequency (0.32×10^{-2} s^{-1} $< N <$ 1.45×10^{-2} s^{-1}). The model results show that the ice motion exhibits two bifurcations. First, it bifurcates into decaying or growing mode, which depends in most cases on the mean surface temperature difference DT_0 representing the strength of the forcing. When DT_0 is small, the decaying mode exists. However, when DT_0 exceeds a first critical value which depends on H_i and N (i.e. when $N = 1.45 \times 10^{-2}$ s^{-1} and $H_i = 2.5$ m, this critical value is 5°C), the growing mode appears. Second, the growing mode bifurcates into non-oscillatory and oscillatory states depending on DT_0 and the properties of ice. If DT_0 exceeds the first critical value but does not reach a second critical value which mostly depends on N (i.e. when $N = 1.45 \times 10^{-2}$ s^{-1}, the second critical value is 14°C), and when ice is thin (generally during summer) the ice motion is non-oscillatory; however, when ice is thick (generally during winter) the ice motion is oscillatory. If DT_0 exceeds the second critical value, only the non-oscillatory growing mode appears. We also estimate the scale of the ice velocity and compute the growth rate and oscillatory period. These values

agree well with the observations and should provide a possible way to predict MIZ migration.

Key words: marginal ice zone, free ice drift, thermally forced air flow, instability, oscillation, ice–air interaction

1 Introduction

The aim of this study is to investigate the generation of strong along-ice-edge winds, the fomation of ice-edge jet, and the instability criteria of ice drift in the MIZ by means of a coupled ice–air model. Ice-drift observations in the Greenland Sea from 1978 April 28 to September 3 (Fig. 1) show two different types of ice motion: oscillation and non-oscillation. Although ocean eddies probably produce oscillations in drift track, another mesoscale mechanism to cause the ice motion may still exist.

A possible mechanism for the mesoscale air–ice interaction is presented in Fig. 2. The low-level air flow generated by the surface temperature gradient is waterward (icebreeze) and equatorward along the ice edge in both eastern Greenland and eastern Antarctic Peninsula, and influences the ice through surface air stress. However, movement of the ice edge in the MIZ changes thermal conditions near the surface and produces an extra air surface temperature gradient across the ice edge.

The ice–air interaction model depicted in the subsequent sections is intended to simulate the main physical processes and to determine some instability criteria for the prediction of MIZ migration.

2 Thermally forced boundary layer air flow

The surface isotherms, which are nearly parallel to the eastern coast of Greenland over the Greenland Sea (Prik 1959), indicate that air temperature increases monotonically waterward near the MIZ. Such a surface temperature gradient will generate a local air flow near the MIZ. In this section we utilize a planetary boundary layer model treated by Kuo (1973) and

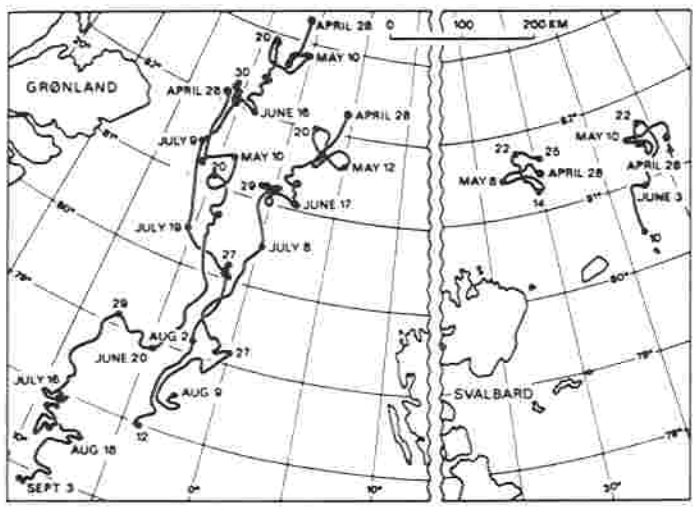

Figure 1. Ice-drift observations in the Greenland Sea.

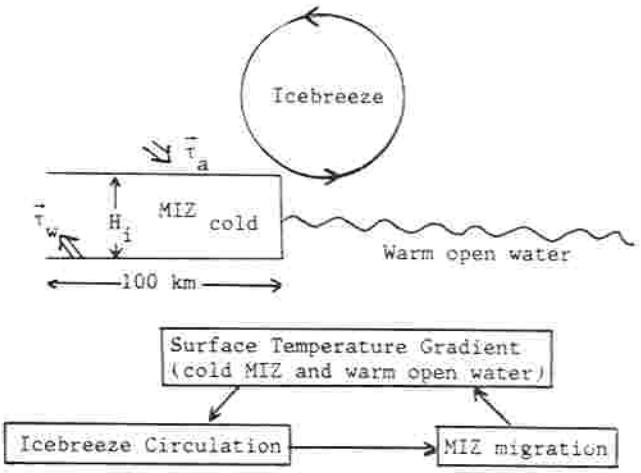

Figure 2. Ice–air–water coupled system.

Chu (1985) to simulate a thermally forced boundary layer air flow. The coordinate system is chosen as moving with the edge of MIZ. The x-axis is in the cross-edge direction, and the y-axis parallel to the ice edge, as shown in Fig. 3. The x-coordinate's unit length is twice the MIZ width, L (200 km), and that of the vertical coordinate is $\delta = (\nu/\Omega)^{1/2}$, where ν is the vertical eddy viscosity, and Ω the angular velocity of the Earth's rotation. The line $x = 1/2$ is located at the ice edge. The MIZ covers the zone $(0 < x < 0.5, y)$ where the y-axis ($x = 0$) is near the boundary between the MIZ and the interior ice pack. It is considered that spatial variations in the MIZ are much larger perpendicular to the ice edge than parallel to it, and hence derivatives with respect to y are assumed to be zero (Lepparanta & Hibler 1986). Since acceleration of the ice edge is small compared with that of the air flow, we may ignore the inertial force due to the use of a coordinate system moving relative to the Earth.

The potential temperature of air is divided into two parts: a basic state $\theta_{B*}(z)$ and perturbation θ'_*. The basic state is given by

$$\theta_{B*}(z) = \theta_{B0} + (N^2 \theta_{B0} \delta / g)\, z, \tag{1}$$

where θ_{B0} is the basic air potential temperature at the surface, and N the Brunt–Väisälä frequency.

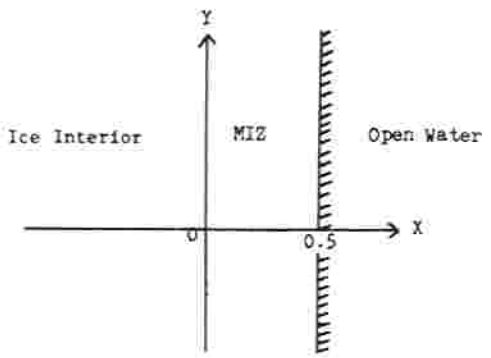

Figure 3. The model MIZ and the coordinate system.

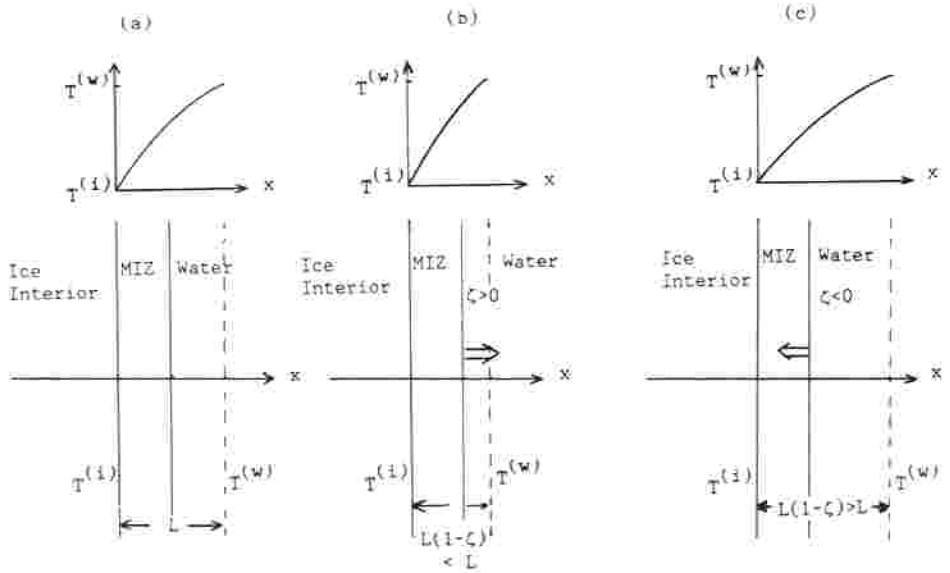

Figure 4. Influence of MIZ migration on surface temperature gradient.

Fig. 4 shows the influence of ice motion on the surface temperature gradient, where $T^{(W)}$ is the water surface temperature at a distance of $L/2$ from the ice edge when the ice is motionless, $T^{(i)}$ is the ice temperature at the boundary between the MIZ and the interior ice, and $L/2$ is the width of the MIZ. The first-order approximation representing the influence of ice migration on surface heating is obtained from the following assumptions: (a) due to the large heat capacity of water, the ice motion does not immediately change the water surface temperature $T^{(W)}$; (b) $T^{(i)}$, which is determined by the large-scale processes, remains constant; (c) the sinusoidal form (as distinct from scale variation) of the surface temperature distribution between $T^{(W)}$ and $T^{(i)}$ remains invariant when the MIZ migrates iceward or waterward.

Waterward/iceward migration of the MIZ shortens/enlarges the distance between $T^{(W)}$ and $T^{(i)}$. The surface temperature gradient is thereby increased/decreased (Fig. 4b, c). Thus the surface temperature perturbation is parameterized as

$$\theta'_*(x, 0, t) = -DT_0\ [1 + \zeta(t)]\ \cos \pi x, \tag{2}$$

where DT_0 is the mean surface temperature difference across the MIZ, and $\zeta(t)$ is the non-dimensional displacement of the ice edge. The coordinates and atmospheric variables are non-dimensionalized by setting

$$(x_*, z_*, t_*) = (xL, z\delta, tT), \qquad s' \equiv \theta'_*/\theta_{B0} = (DT_0/\theta_{B0})s,$$
$$(u_*, v_*, w_*) = U(u, v, w\delta/L), \qquad P_* = (g\delta DT_0/\theta_{B0})p, \tag{3}$$

where

$$U \equiv g\delta DT_0/(2L\Omega\theta_{B0}) \tag{4}$$

is the scale of icebreeze wind, and T is the time-scale for the change of surface temperature gradient due to the movement of the ice edge. If we assume that the local air flow satisfies the modified Boussinesq approximation (Kuo 1973), the vorticity equation, the momentum

equation (both in the y direction), and the heat equation for the air disturbances generated by differential surface temperature gradient near the MIZ (written in dimensionless variables) are (Chu 1985)

$$E\nabla_v^2\nabla^2\psi = f_0\,\partial v/\partial z - \partial s/\partial x, \tag{5}$$

$$E\nabla_\nu^2 v = -f_0\,\partial\psi/\partial z, \tag{6}$$

and

$$E\nabla_\nu^2 s = R_i\,\partial\psi/\partial x. \tag{7}$$

In the foregoing,

$$u = -\partial\psi/\partial z, \qquad w = \partial\psi/\partial x$$

$$\nabla_\nu^2 \equiv \delta^2\nu_h/(L^2\nu)\,\partial^2/\partial x^2 + \partial^2/\partial z^2, \qquad \nabla^2 \equiv \delta^2/L^2\,\partial^2/\partial x^2 + \partial^2/\partial z^2, \tag{8}$$

where $f_0 = \sin\phi$, ϕ is the latitude, ν_h is the horizontal eddy viscosity, and

$$E \equiv \nu/(2\Omega\delta^2) = 1/2, \qquad R_i \equiv \delta^2 N^2/(4L^2\Omega^2) \tag{9}$$

are the Ekman and global Richardson numbers respectively. Non-linear terms are dropped because the Rossby number is much less than unity, and terms involving time derivatives are dropped because $2\Omega T \gg 1$. Eliminating v and s from (5)–(7) we find that the stream function satisfies the following partial differential equation:

$$(1/4\nabla_\nu^4 + f_0^2)\,\partial^2\psi/\partial z^2 + R_i\,\partial^2\psi/\partial x^2 = 0. \tag{10}$$

We solve (10) for the stream function ψ, and obtain the solutions of v and s from (6) and (7) after substituting ψ. The local air flow is thermally forced by the surface temperature gradient as indicated in (2), therefore the stream function should be written by

$$\psi(x, z, t) = \bar{\psi}(z, t)\sin\pi x. \tag{11}$$

The boundary conditions in the vertical direction are derived as follows. The dependent variables should remain finite as $z \to \infty$, i.e.

$$\lim_{z\to\infty}(|\psi|, |\partial\psi/\partial z|, |v|, |s|) < \infty. \tag{12}$$

The boundary conditions at $z = 0$ are:

$$\psi = 0, \qquad \partial\psi/\partial z = K\,\partial^2\psi/\partial z^2,$$

$$v = K\,\partial v/\partial z, \qquad s = -[1 + \zeta(t)]\cos\pi x, \tag{13}$$

where K is a measure of the effective depth of the constant stress sublayer (Kuo 1971). Substituting (11) into (10) we obtain the following sixth-order ordinary differential equation for the Fourier coefficient $\bar{\psi}$:

$$d^6\bar{\psi}/dz^6 - 4\gamma\,d^4\bar{\psi}/dz^4 + 4(f_0^2 + \gamma^2)d^2\bar{\psi}/dz^2 - 4\pi^2 R_i\bar{\psi} = 0, \tag{14}$$

where

$$\gamma \equiv \pi^2\delta^2\nu_h/(2L^2\nu). \tag{15}$$

The general solution of (14) has the following form:

$$\bar{\psi}(z, t) = [1 + \zeta(t)]\sum_{j=1}^{6}\bar{a}_j\exp(\lambda_j z), \tag{16}$$

Table 1. The standard model parameters.

$L = 200$ km,	$\nu = 5\ m^2\ s^{-1}$,	$\nu_h = 10^5\ m^2\ s^{-1}$,
$\Omega = 0.7292 \times 10^{-4}\ s^{-1}$,	$g = 9.81\ m\ s^{-2}$,	$K = 0.9$,
$\theta_{B0} = 270$ K,	$C'_w = 0.55\ kg\ m^{-2}\ s^{-1}$,	$C_a = 3 \times 10^{-3}$,
$\rho_a = 1.29\ kg\ m^{-3}$,	$\rho_w = 10^3\ kg\ m^{-3}$.	$\rho_i = 910\ kg\ m^{-3}$.
$\phi = (65^\circ, 70^\circ, 75^\circ)$.		

where the eigenvalues $\lambda_j (j = 1, 2, \ldots, 6)$ are the roots of the sixth-order algebraic equation:

$$\lambda^6 - 4\gamma\lambda^4 + 4(f_0^2 + \gamma^2)\lambda^2 - 4\pi^2 R_i = 0. \tag{17}$$

Table 1 lists the parameter values for the present calculation, and Table 2 lists all the eigenvalues for typical stratification at three distinct latitudes (65°, 70°, and 75°). Notice that f_0^2 appears in (17), so the eigenvalues in Table 2 represent both northern and southern polar regions. According to the upper boundary conditions listed in (12) we must set equal to zero all coefficients $\bar{a}_j$ which correspond to eigenvalues with positive real parts. Consequently the general solution (16) satisfying the top boundary conditions may be written:

$$\bar{\psi}(z, t) = [1 + \zeta(t)] \sum_{j=1}^{3} \bar{a}_j \exp(\lambda_j z), \tag{18}$$

where the eigenvalues λ_j will have negative real parts. Substituting (18) into (11) we obtain the stream function

$$\psi(x, z, t) = \sum_{j=1}^{3} \bar{a}_j [1 + \zeta(t)] \exp(\lambda_j z) \sin \pi x. \tag{19}$$

Integrating the momentum equation (6) and the heat equation (7) with respect to z after substituting (19), we find that v and s are given by

$$v(x, z, t) = \left[\bar{b} \exp(-\sqrt{2\gamma}\, z) - f_0 \sum_{j=1}^{3} \bar{a}_j \lambda_j F(\lambda_j, \gamma) \exp(\lambda_j z) \right] [1 + \zeta(t)] \sin \pi x. \tag{20}$$

$$s(x, z, t) = \left[\bar{c} \exp(-\sqrt{2\gamma}\, z) + \pi R_i \sum_{j=1}^{3} \bar{a}_j F(\lambda_j, \gamma) \exp(\lambda_j z) \right] [1 + \zeta(t)] \cos \pi x, \tag{21}$$

where

$$F(\lambda, \gamma) \equiv 1/(\lambda^2/2 - \gamma). \tag{22}$$

Substituting the solutions (19)–(21) into the vorticity equation (5) we find that

$$\bar{c} = \sqrt{2\gamma}\, f_0\, \bar{b}/\pi. \tag{23}$$

Table 2. The eigenvalues of the boundary layer air flow model at three different latitudes.

Latitudes		
65°	70°	75°
(−0.32371, 0)	(−0.31223, 0)	(−0.30378, 0)
(−1.02800, 0.87796)	(−1.04508, 0.89586)	(−1.05823, 0.90973)
(−1.02800, −0.87796)	(−1.04508, −0.89586)	(−1.05823, −0.90973)
(0.32371, 0)	(0.31223, 0)	(0.30378, 0)
(1.02880, 0.87796)	(1.04508, 0.89586)	(1.05823, 0.90973)
(1.02800, −0.87796)	(1.04508, −0.89586)	(1.05823, −0.90973)

Substituting the solutions (19)–(21) into the surface boundary conditions listed in (13) we obtain the following four algebraic equations for $\bar{a}_j$ and $\bar{b}$.

$$\sum_{j=1}^{3} \bar{a}_j = 0. \tag{24}$$

$$\sum_{j=1}^{3} \lambda_j (1 - K\lambda_j)\, \bar{a}_j = 0, \tag{25}$$

$$-f_0 \sum_{j=1}^{3} \lambda_j (1 - K\lambda_j)\, F(\lambda_j, \gamma)\, \bar{a}_j + \bar{b}(1 + K\sqrt{2\gamma}) = 0, \tag{26}$$

$$\pi R_1 \sum_{j=1}^{3} F(\lambda_j, \gamma)\, \bar{a}_j + \sqrt{2\gamma} f_0 \bar{b}/\pi = -1. \tag{27}$$

The four constants $\bar{a}_1$, $\bar{a}_2$, $\bar{a}_3$, and $\bar{b}$ can be readily obtained by solving these four linear inhomogeneous algebraic equations.

Figs 5–7 display the solutions for zero ice motion at $\phi = 75°$, $DT_0 = 6°C$, and $N = 10^{-2}$ s^{-1}. Fig. 5 shows the distribution of air temperature in the cross-ice section. The horizontal temperature gradient is very deep near the ice-edge and decreases with altitude. Above $z = 3$ ($z_* = 800$ m) there is almost no horizontal temperature gradient. Fig. 6 shows the distribution of the wind v along the ice edge in the cross-ice section. The longshore wind is equatorward at low-levels (below $z = 2$) and poleward at high-levels. This strong equatorward wind along the ice-edge near the MIZ (around 7 m s^{-1}) is consistent with the observations near the Antarctic Peninsula (Schwerdtfeger 1979). Fig. 7 shows the cross-ice

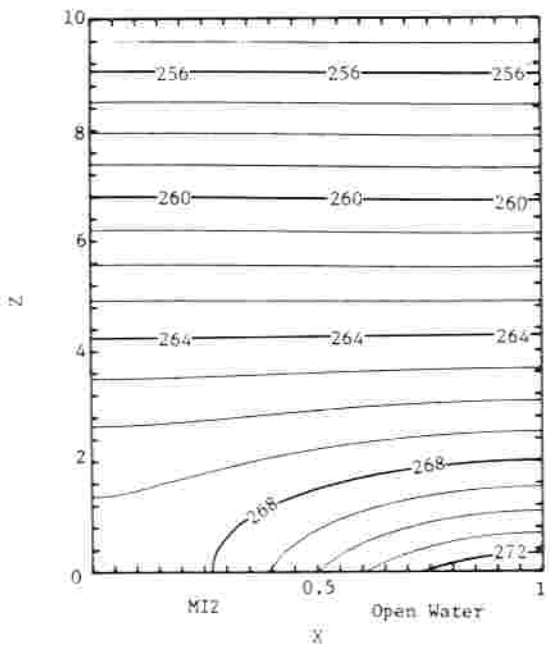

Figure 5. The distribution of air temperature (K) in the cross-ice section.

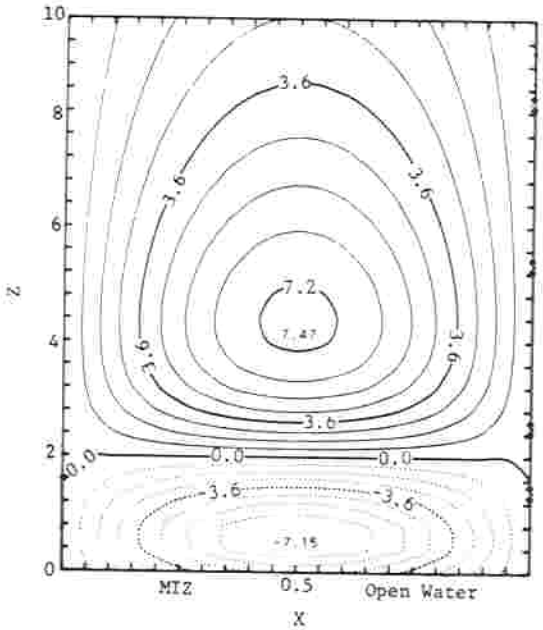

Figure 6. The distribution of thermally forced along ice-edge winds (m s^{-1}) in the cross-ice section.

circulation. We see the obvious icebreeze at low levels. The speed of the icebreeze reaches a maximum (which is around 3 m s^{-1}) at the ice-edge.

3 Free ice drift model

The linearized momentum equations for a free drift ice model are written by:

$$\partial u_i/\partial t_* = fv_i + (\tau_{ax} + \tau_{wx})/(\rho_i H_i), \tag{28}$$

$$\partial v_i/\partial t_* = -fu_i + (\tau_{ay} + \tau_{wy})/(\rho_i H_i), \tag{29}$$

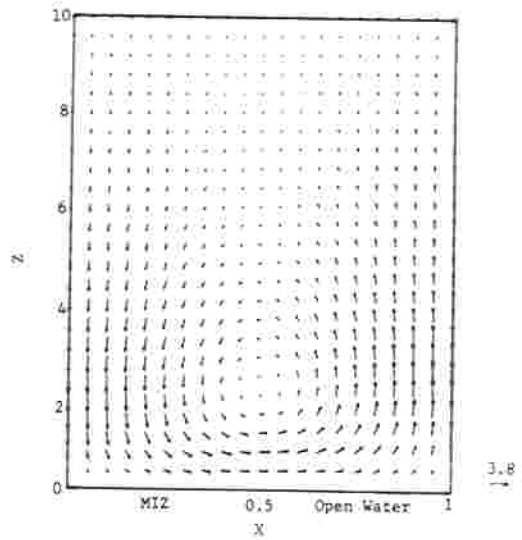

Figure 7. Thermally forced icebreeze circulation in the cross-ice section with u in m s^{-1} and w in cm s^{-1}.

where $f(=2\Omega \sin \phi)$ is the Coriolis parameter, H_i the mean ice thickness, ρ_i the ice density, $\mathbf{V}_i = (u_i, v_i)$ the ice velocity, $\boldsymbol{\tau}_a = (\tau_{ax}, \tau_{ay})$ the wind stress, $\boldsymbol{\tau}_w = (\tau_{wx}, \tau_{wy})$ the water stress, x the non-dimensional horizontal coordinate. The air and water stresses are given by

$$\boldsymbol{\tau}_a = C_a' \mathbf{V}_a, \qquad \boldsymbol{\tau}_w = C_w' (\mathbf{V}_w - \mathbf{V}_i), \tag{30}$$

where $\mathbf{V}_a$ is the surface air velocity, $\mathbf{V}_w$ the surface water velocity and C_a' and C_w' the dimensional air and water drag coefficients. C_a' is further given by

$$C_a' = C_a \rho_a U[(\partial \psi/\partial z)^2 + v^2]^{1/2}|_{z=0,\, x=0.5,\, \xi=0}, \tag{31}$$

where ψ and v are obtained by (19)–(20). In contrast to the treatments by Hibler (1984), and by Lepparanta & Hibler (1986), the surface air stress $\boldsymbol{\tau}_a$ is directly computed by the boundary-layer flow model presented in the previous section. Substituting the expressions for air and water stresses (30) into (28) and (29) and assuming that $\mathbf{V}_w = 0$, we obtain

$$\partial u_i/\partial t_* = -\bar{C}_w u_i + f v_i + \bar{C}_a u_{a0}[1 + \xi(t)] \sin \pi x, \tag{32}$$

$$\partial v_i/\partial t_* = -\bar{C}_w v_i - f u_i + \bar{C}_a v_{a0}[1 + \xi(t)] \sin \pi x, \tag{33}$$

where

$$\bar{C}_a \equiv C_a'/(\rho_i H_i), \qquad \bar{C}_w \equiv C_w'/(\rho_i H_i),$$

$$u_{a0} \equiv -g\delta DT_0/(2L\Omega\theta_{B0}) \sum_{j=1}^{3} \bar{a}_j \lambda_j,$$

$$v_{a0} \equiv g\delta DT_0/(2L\Omega\theta_{B0}) \left[\bar{b} - f_0 \sum_{j=1}^{3} \bar{a}_j \lambda_j F(\lambda_j, \gamma)\right]. \tag{34}$$

Equations (32) and (33) are the basic equations for ice motion.

4 Wind-driven steady-state ice motion (u_{is}, v_{is})

For the steady-state, the basic equations (32) and (33) become

$$-\bar{C}_w u_{is} + f v_{is} + \bar{C}_a u_{a0} \sin \pi x = 0, \tag{35a}$$

$$-\bar{C}_w v_{is} - f u_{is} + \bar{C}_a v_{a0} \sin \pi x = 0. \tag{35b}$$

Since our model is linear the mechanically forced ice motion u_{is} and v_{is} should have the same Fourier component as the forcing terms, i.e.

$$u_{is}(x) = \bar{u}_{is} \sin \pi x, \qquad v_{is}(x) = \bar{v}_{is} \sin \pi x \tag{36}$$

Substituting (36) into (35a, b) we find that

$$\bar{u}_{is} = \bar{C}_a(\bar{C}_w u_{a0} + f v_{a0})/(\bar{C}_w^2 + f^2), \tag{37a}$$

$$\bar{v}_{is} = \bar{C}_a(\bar{C}_w v_{a0} - f u_{a0})/(\bar{C}_w^2 + f^2). \tag{37b}$$

We can take $\bar{u}_{is}$ and $\bar{v}_{is}$ as scales for the ice velocities. At $N = 10^{-2}\ s^{-1}$, $DT_0 = 10°C$, and $H_i = 1.5$ m, we find that

$$\bar{u}_{is} = 13.3 \text{ cm s}^{-1}, \qquad \bar{v}_{is} = -54.1 \text{ cm s}^{-1},$$

which agree with the observations of ice speeds in the Greenland Sea and Arctic Ocean.

5 Wind-driven time-dependent ice motion (u_i, v_i)

5.1 SOLUTIONS

As in the steady-state case, the solutions of the basic equations (32) and (33) should have the same Fourier component as the forcing terms, i.e.

$$u_i(x, t_*) = \bar{u}_i(t_*) \sin \pi x, \qquad v_i(x, t_*) = \bar{v}_i(t_*) \sin \pi x. \tag{38}$$

By definition, $\zeta(t)$ is the non-dimensional ice-edge displacement in the x-direction. It is related to ice velocity by

$$L d\zeta/dt_* = u_i(1/2, t_*) = \bar{u}_i(t_*). \tag{39}$$

Eliminating one of the two dependent variables $\bar{u}_i$ and $\bar{v}_i$ from (32) and (33) we get the following third-order equation for the coefficients:

$$[D^3 + 2\bar{C}_w D^2 + (\bar{C}_w^2 - \bar{C}_a u_{a0}/L + f^2)D - \bar{C}_a \bar{C}_w u_{a0}/L - f\bar{C}_a v_{a0}/L]\ (\bar{u}_i, \bar{v}_i) = 0, \tag{40}$$

where

$$D = d/dt_*. \tag{41}$$

The general solutions of (40) have the following form:

$$\bar{u}_i(t_*) = \sum_{j=1}^{3} d_j \exp(\mu_j t_*), \qquad \bar{v}_i(t_*) = \sum_{j=1}^{3} e_j \exp(\mu_j t_*). \tag{42}$$

The eigenvalues μ_1, μ_2, μ_3 are the roots of the following cubic equation:

$$\mu^3 + 2\bar{C}_w \mu^2 + (\bar{C}_w^2 - \bar{C}_a u_{a0}/L + f^2)\mu - (\bar{C}_a/L)(\bar{C}_w u_{a0} + f v_{a0}) = 0. \tag{43}$$

5.2 STABILITY AND OSCILLATION CRITERIA

The standard values of parameters are given in Table 1. We solve the characteristic equation (43) with different values of H_i, N, and DT_0. H_i varies from 0.5 to 10.5 m, N from 0.32×10^{-2} to 1.45×10^{-2} s^{-1}, DT_0 from 1° to 21°C. The instability criterion for MIZ migration in the ice–air coupled model can be written

$$\mathrm{Re}(\bar{\mu}) \begin{cases} < 0 & \text{decaying} \\ = 0 & \text{neutral} \\ > 0 & \text{growing} \end{cases} \qquad \bar{\mu} = \mu_1, \mu_2, \mu_3 \tag{44}$$

where $\bar{\mu}$ is the root of cubic equation (43). The oscillation criterion for MIZ migration is given by

$$\mathrm{Im}(\bar{\mu}) \begin{cases} = 0 & \text{non-oscillatory} \\ \neq 0 & \text{oscillatory} \end{cases} \qquad \bar{\mu} = \mu_1, \mu_2, \mu_3. \tag{45}$$

5.3 DEPENDENCE OF EIGENVALUES μ_1, μ_2, AND μ_3 ON THE PARAMETERS (H_i, N, DT_0)

We compute all the roots of (43) for different values of the parameters H_i, N, DT_0, and obtain three roots μ_1, μ_2, μ_3 at each point of the parameter space (H_i, N^2, DT_0). Here μ_1 is

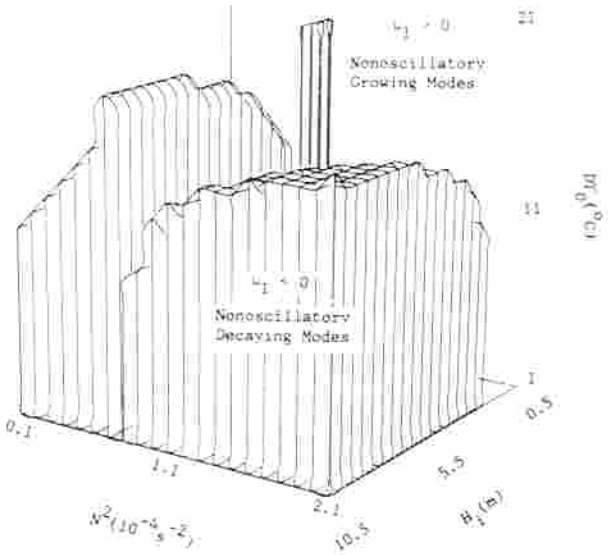

Figure 8. Separation of non-oscillatory decaying and growing modes referring to real eigenvalue μ_1.

real throughout that space, and μ_2 and μ_3 are real for some values of (H_i, N^2, DT_0) and are complex elsewhere.

Fig. 8 shows the surface $\mu_1 = 0$ in the three-dimensional space (H_i, N^2, DT_0). This surface divides the space into two parts corresponding to growing and decaying modes. The growing mode generally appears when DT_0 exceeds some critical value around 10°C. This critical value decreases with H_i, and becomes very small (around 1°C) in the region of small mean ice-thickness H_i ($H_i < 1.5$ m). Ice motion corresponding to the eigenvalue μ_1 is non-oscillatory.

Fig. 9 indicates the surface of $\mathrm{Re}(\mu_2) = 0$ (or $\mathrm{Re}(\mu_3) = 0$) in the parameter space (H_i, N^2, DT_0). This surface separates the whole space into growing and decaying parts. The growing mode is present when DT_0 exceeds some critical value which is a function of H_i and N^2 (when $H_i = 4.5$ m and $N^2 = 1.1 \times 10^{-4}$ s^{-2}, $DT_0 = 3$°C), and is in the region that the mean ice thickness H_i exceeds some critical value around 2.5 m.

Fig. 10 reveals the segregation of non-oscillatory and oscillatory modes relating to μ_2 and μ_3. Comparing Fig. 10 with Fig. 9, we find that the decaying mode of μ_2 and μ_3 is generally non-oscillatory whereas the growing mode of μ_2 and μ_3 is generally oscillatory.

Figs 8–10 show the following: (1) both non-oscillatory and oscillatory decaying modes share a common area (restricted to the region of small DT_0) in the parameter space; however, (2) non-oscillatory and oscillatory growing modes occupy different regions in the parameter space. The segregation of the two modes depends largely on DT_0 and H_i.

Whether ice motion grows or decays substantially depends on a first critical value of the parameter DT_0 (when $N = 1.45 \times 10^{-2}$ s^{-1} and $H_i = 2.5$ m, this critical value is 5°C). When DT_0 is smaller than the first critical value, the motive force is so small that it cannot overcome dissipative effects and does not make ice motion unstable. If DT_0 becomes large enough to overcome the dissipative effects of friction, ice motion becomes larger.

Whether ice motion is oscillatory or non-oscillatory largely depends on DT_0 and the properties of ice. If DT_0 exceeds the first critical value but does not reach a second critical value which mostly depends on N (i.e. when $N = 1.45 \times 10^{-2}$ s^{-1}, the second critical value is

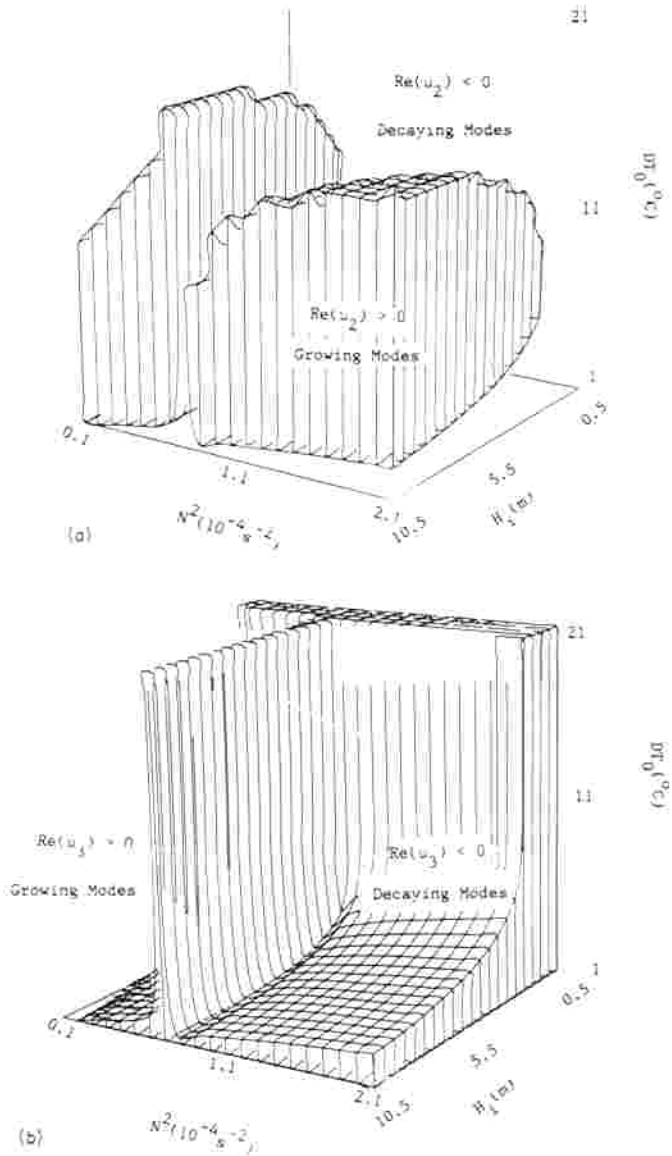

Figure 9. Separation of decaying and growing modes referring to eigenvalues μ_2 and μ_3.

14°C), and when ice is thin (generally during summer) the ice motion is non-oscillatory, however, when the ice is thick (generally during winter) the ice motion is oscillatory. If DT_0 exceeds the second critical value, only the non-oscillatory growing mode appears.

6 Non-oscillatory growing mode

The non-oscillatory growing mode of ice motion is due to the positive eigenvalue μ_1. Fig. 11 indicates the isolines of μ_1 with H_i and DT_0 at two different values of N (0.32×10^{-2} s^{-1}, 1.45×10^{-2} s^{-1}). The isoline patterns at these two values are very similar. A 'Γ-type'

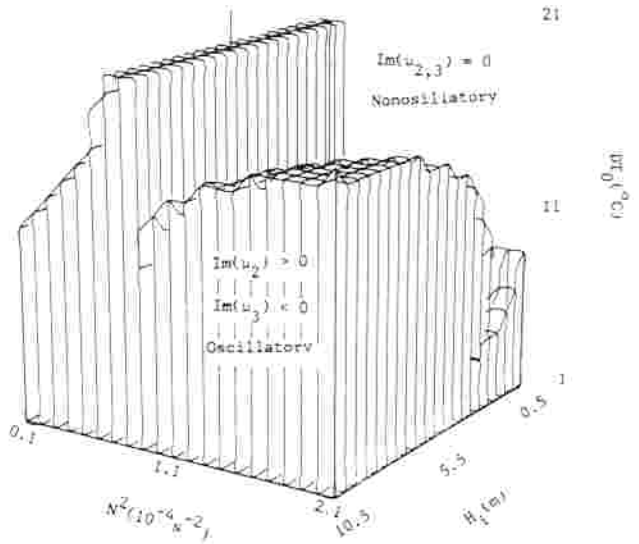

Figure 10. Separation of non-oscillatory and oscillatory states referring to eigenvalues μ_2 and μ_3.

boundary separates the non-oscillatory growing ($\mu_1 > 0$) and decaying ($\mu_1 < 0$) modes. The growing mode is located either in an area of large DT_0 ($DT_0 > 10^\circ$C if $N = 0.32 \times 10^{-2}$ s^{-1} and $DT_0 > 14^\circ$C if $N = 1.45 \times 10^{-2}$ s^{-1}) or in an area of small H_i when DT_0 is small. In the growing area the growth rate accelerates monotonically with an increase of DT_0. It is quite understandable that the larger DT_0 is, the stronger the forcing.

For the non-oscillatory growing mode the time during which the ice doubles its speed is

$$T_1 = \ln 2/\mu_1, \qquad (\mu_1 > 0). \tag{46}$$

If H_i and N are assigned values

$H_i = 1$ m, $\qquad N = 10^{-2}$ s^{-1},

the doubling time treated as a function of DT_0 is shown in Fig. 12, which displays a decrease of T_1 with an increase of DT_0. T_1 changes from 2.2 to 0.18 hr as DT_0 varies from 5° to 22°C.

7 Oscillatory growing mode

The oscillatory growing mode is ice motion due to μ_2 (or μ_3), whose real part is positive and the imaginary part is different from zero, i.e.

$$\text{Re}\,(\mu_2) > 0 \text{ (or Re}\,(\mu_3) > 0), \qquad \text{Im}\,(\mu_2) \neq 0 \text{ (or Im}\,(\mu_3) \neq 0).$$

Figs 13 and 14 show the isolines of real and imaginary parts of μ_2 and μ_3 with H_i and DT_0 for two different values of N (0.32×10^{-2} s^{-1}, 1.45×10^{-2} s^{-1}). From these figures we find that the growing oscillatory mode is located in the area where DT_0 is larger than the first critical value and smaller than the second critical value. As in the non-oscillatory case the growth rate Re $(\mu_{2,3})$ increases with an increase of DT_0 (increase of forcing). With $DT_0 = 6^\circ$C, $N = 0.32 \times 10^{-2}$ s^{-1}, and $H_i = 5.5$ m, the growth rate

$$\text{Re}\,(\mu_{2,3}) = 0.15 \times 10^{-2} \text{ s}^{-1}.$$

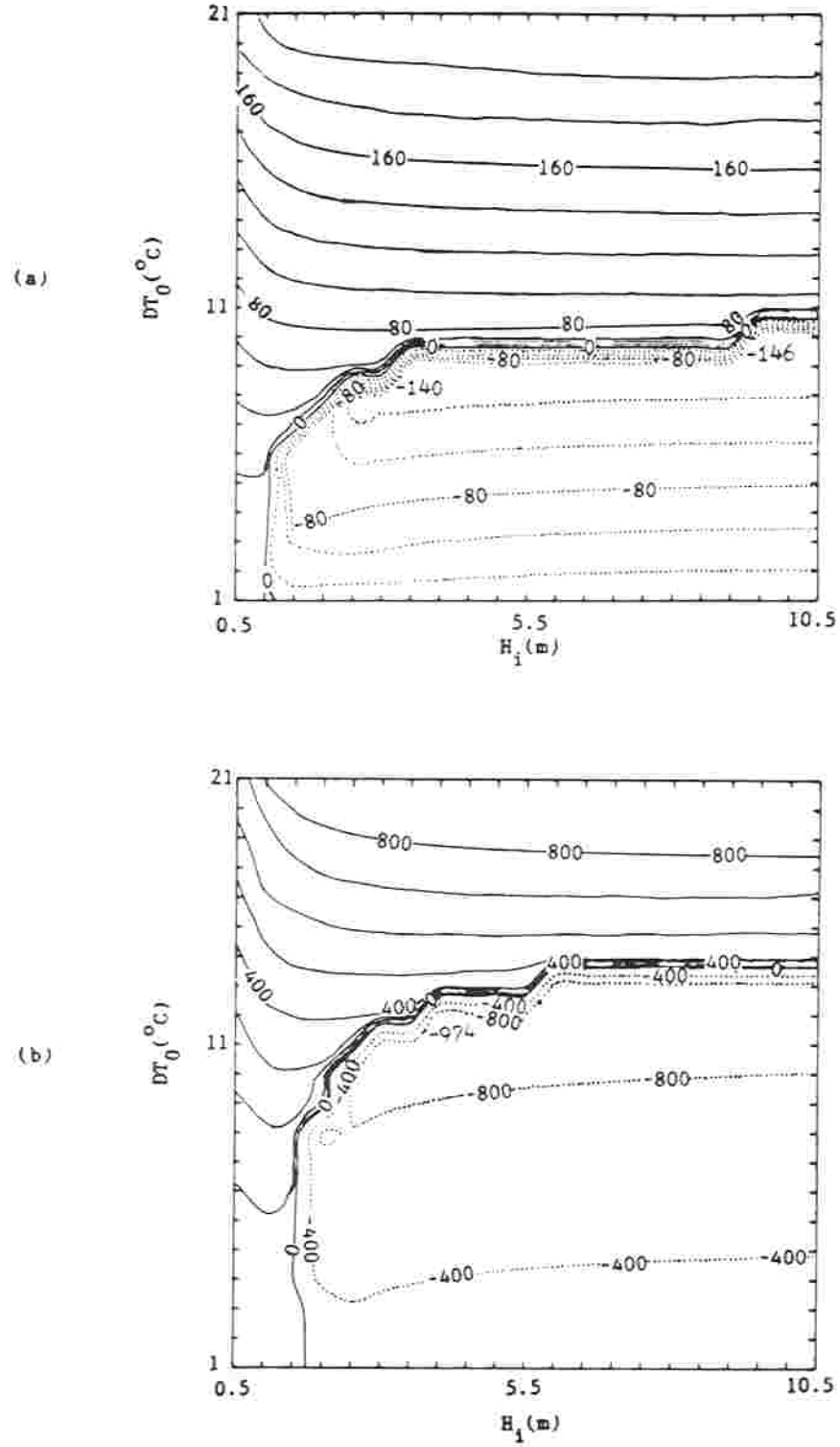

Figure 11. Isolines of the eigenvalue μ_1.

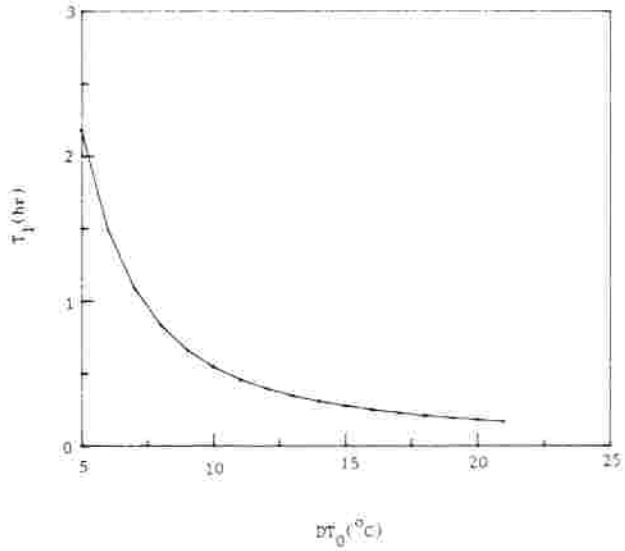

Figure 12. Dependence of doubling time on DT_0 for the non-oscillatory growing mode.

The corresponding doubling time is 12.84 hr. The period of the growing oscillatory mode defined by

$$T_p = 2\pi/|\operatorname{Im}(\mu_{2,3})| \tag{47}$$

is 9.28 hr.

Fig. 15 shows the doubling time and period as functions of DT_0 for $H_i = 5$ m and $N = 10^{-2}\ s^{-1}$. The doubling time decreases monotonically with an increase of DT_0. However, the period increases slightly when DT_0 varies from 5°C to 10°C, and then increases rapidly with DT_0. When $DT_0 = 12.5$°C the period is nearly one day.

8 Conclusions

(a) This ice–air coupled model is intended to depict only the mesoscale processes of ice–air interaction in the MIZ. The synoptic scale pressure gradient associated with the semi-permanent Icelandic low may additionally produce equatorward winds in the Greenland Sea, and large-scale ocean currents near the East Greenland Sea or the Antarctic Peninsula may drive ice-drift. These processes are, however, beyond the scope of this paper. Nevertheless, when the ice-to-open-water temperature gradient is strong, the mesoscale feedback mechanism discussed here may become as strong as, or stronger than, the synoptic scale and oceanic forcings.

(b) The equatorward and waterward surface winds near the MIZ in the Greenland Sea and the east Antarctic Peninsula are thermally generated by differential surface temperature gradient over ice and water. The surface wind has its maximum speed along the ice edge. The component of surface wind parallel to the ice edge can reach 7 $m\,s^{-1}$ when the temperature gradient in the cross-ice direction is chosen as 0.03 $K\,km^{-1}$. This agrees with the observations at the east Antarctic Peninsula reported by Schwerdtfeger (1979).

(c) The migration of the MIZ is forced by local winds generated by differential surface temperature gradient over ice and water near the ice edge. The ice velocity $\mathbf{V}_i$ has the

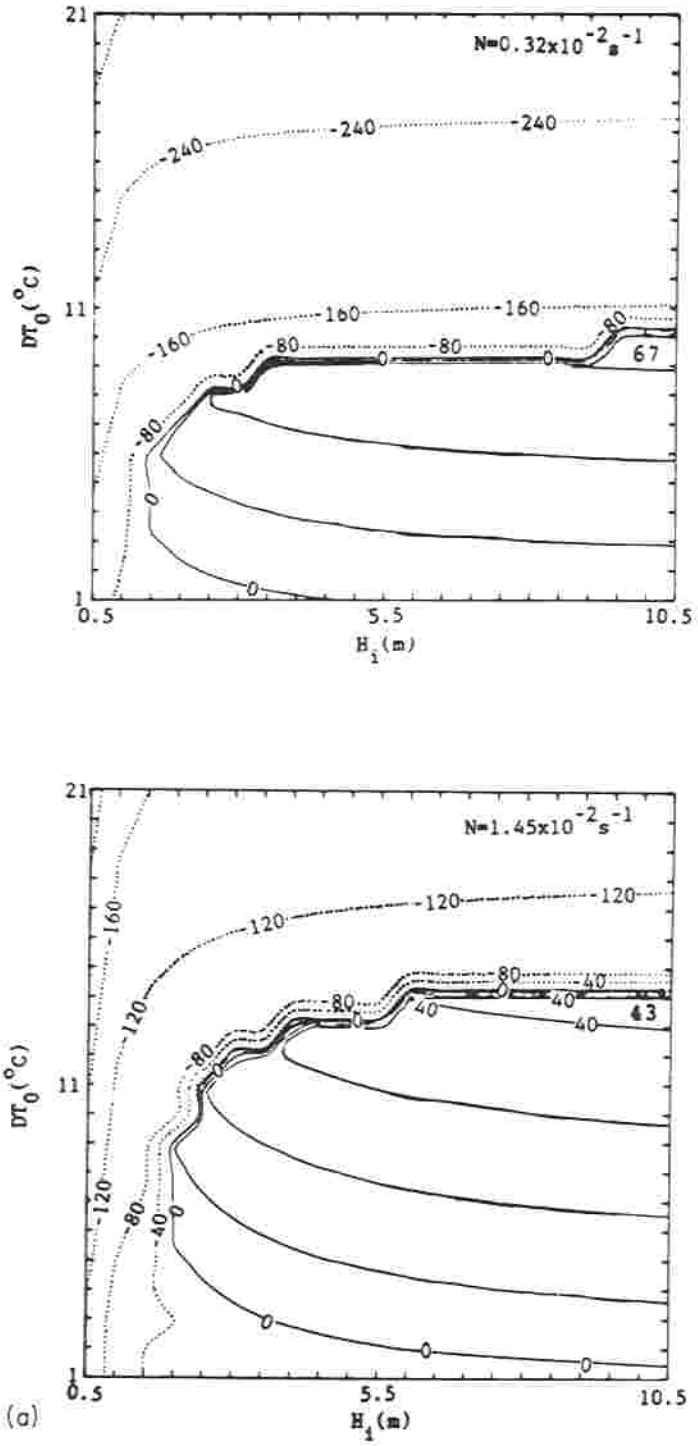

Figure 13. (a) Isolines of the real part of eigenvalue μ_2, (b) isolines of the real part of eigenvalue μ_3.

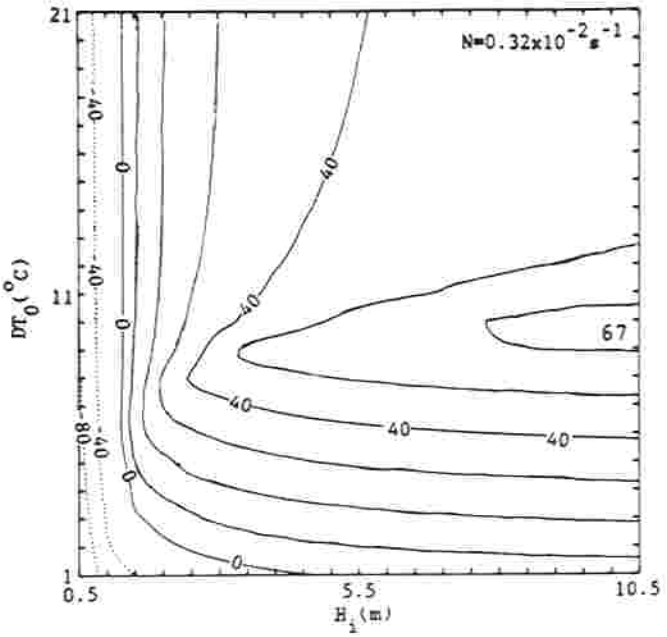

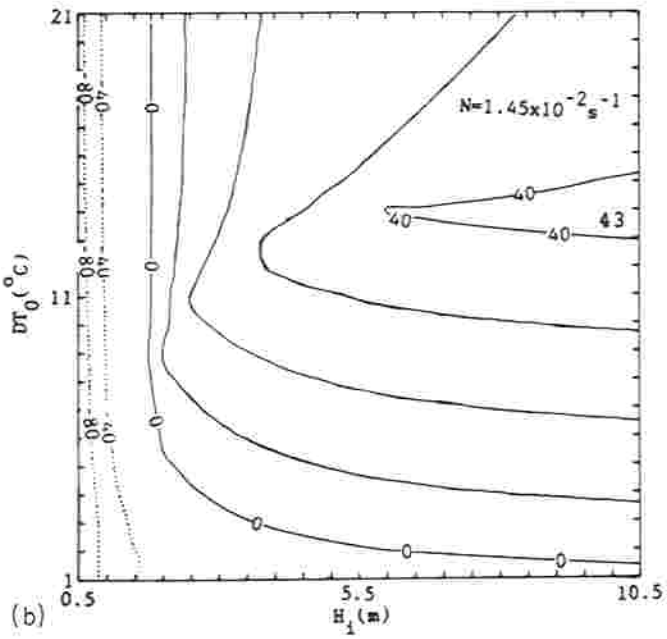

(b)

Figure 13 – *continued*

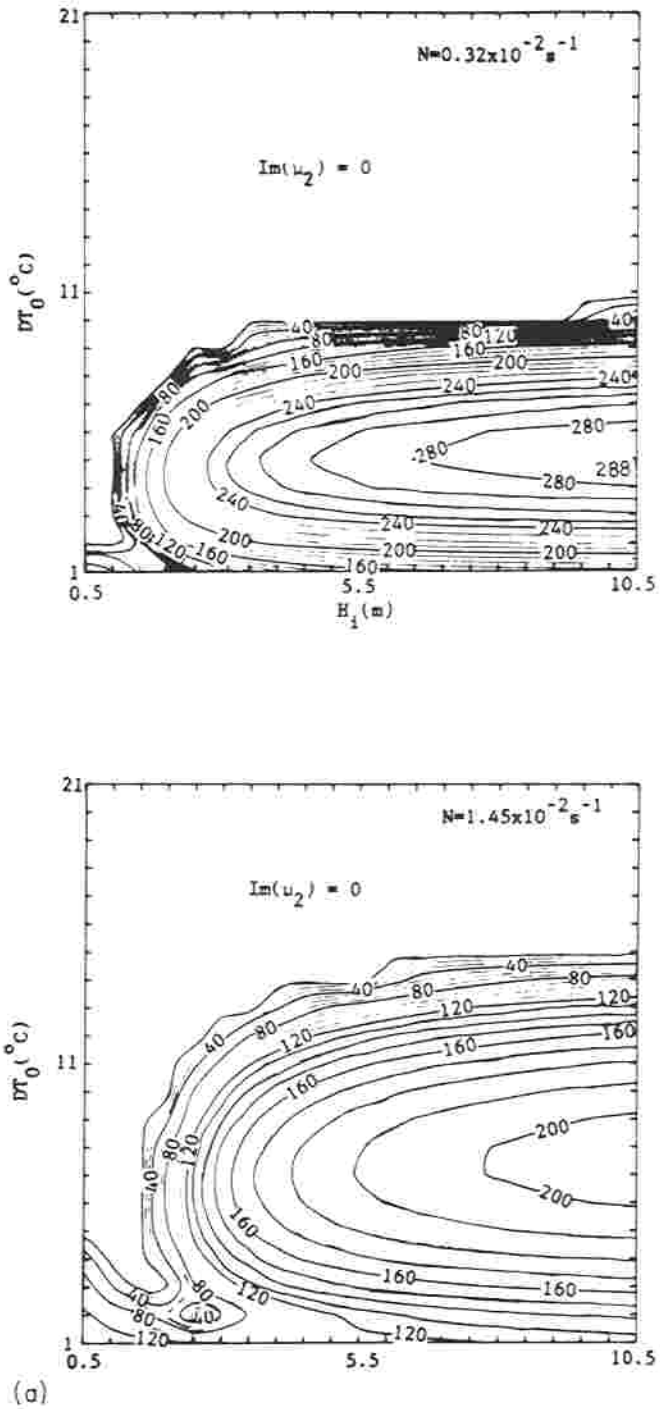

Figure 14. (a) Isolines of the imaginary part of eigenvalue μ_2. (b) isolines of the imaginary part of eigenvalue μ_3.

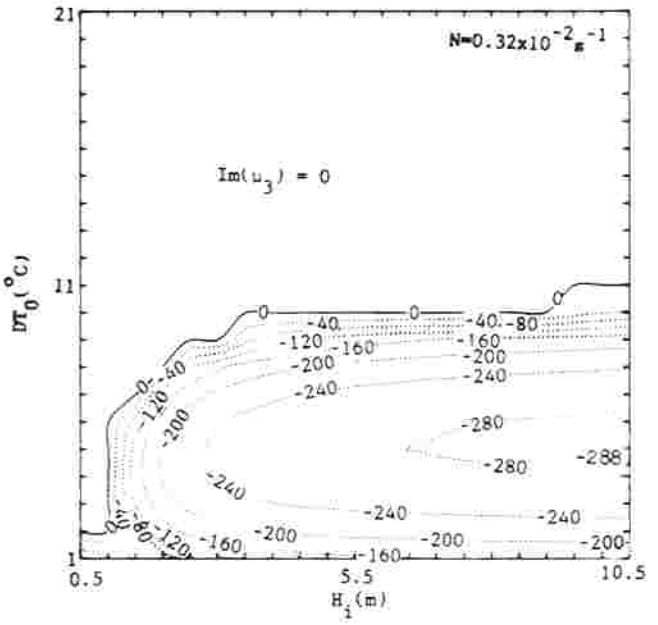

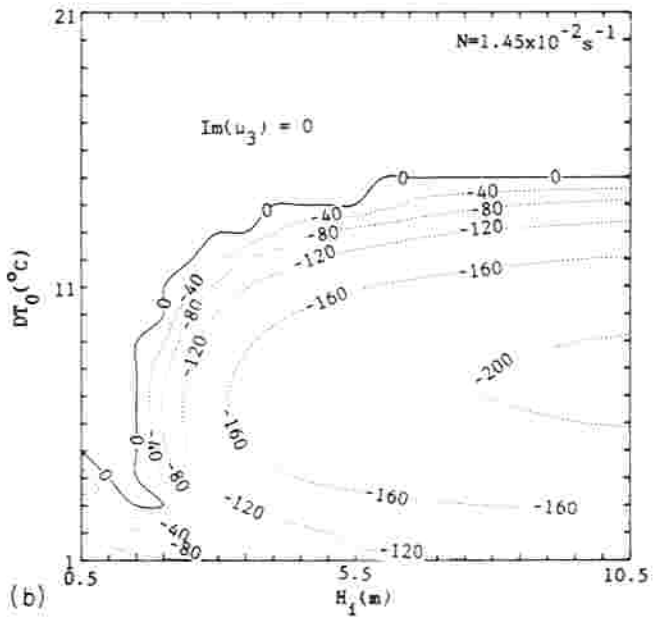

Figure 14 – *continued*

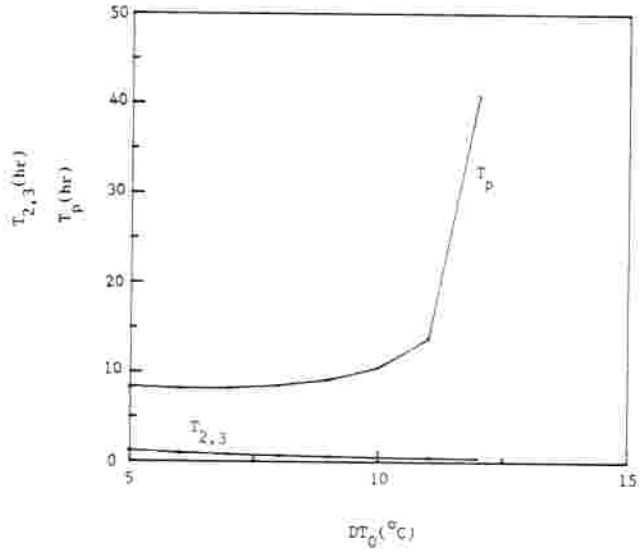

Figure 15. Dependence of doubling time and period on DT_0 for oscillatory growing mode.

sinusoidal form (38) showing an ice-edge jet. The ice velocity has its maximum at the ice edge and decreases iceward. This implies that the ice-edge jet is produced indirectly by the thermal effect of the ice–water contrasts.

(d) The ice motion has two bifurcations. First, it bifurcates into a decaying or growing mode, which depends in most cases on the mean surface temperature difference DT_0 representing the strength of the forcing. When DT_0 is small, the decaying mode exists. However, when DT_0 exceeds a first critical value which depends on H_i and N (i.e. when $N = 1.45 \times 10^{-2}\ s^{-1}$ and $H_i = 2.5$ m, this critical value is 5°C), the growing mode appears. Secondly, the growing mode bifurcates into non-oscillatory and oscillatory states depending on DT_0 and the properties of ice. If DT_0 exceeds the first critical value but does not reach a second critical value which mostly depends on N (i.e. when $N = 1.45 \times 10^{-2}\ s^{-1}$, the second critical value is 14°C), and when ice is thin (generally during summer) the ice motion is non-oscillatory; however, when ice is thick (generally in winter) the ice motion is oscillatory. If DT_0 exceeds the second critical value, only the non-oscillatory growing mode appears.

Acknowledgments

The author is grateful to Professor H. L. Kuo and Professor D. R. MacAyeal of the University of Chicago for invaluable discussion and comments. The reviewers' comments are also highly appreciated.

This research was supported by Grant ATM 83-14206 from the National Science Foundation.

References

Chu, P. C., 1985. A boundary layer theory of coastal desert formation and seabreeze circulation, *PhD thesis*, The University of Chicago.

Hibler, W. D. III, 1984. Ice dynamics, *CRREL Monogr. 84-3*, 52 pp.

Kuo, H. L., 1971. Axisymmetric flows in the boundary layer of a maintained vortex, *J. atmos. Sci.*, **28**, 20–41.

Kuo, H. L., 1973. Planetary boundary layer flow of a stable atmosphere over the globe, *J. atmos. Sci.*, **30**, 53–65.

Lepparanta, M. & Hibler, W. D. III, 1986. On the role of plastic ice interaction in marginal ice zone dynamics, *J. geophys. Res.*, in press.

McPhee, M. G., 1979. The effect of the oceanic boundary layer on the mean drift of pack ice: application of a simple model, *J. Phys. Oceanogr.*, **9**, 388–400.

Overland, J. E., Moţjeld, H. O. & Pease, C. H., 1984. Wind-driven ice drift in a shallow sea, *MIZEX Bull.*, **3**, 49–53.

Pease, C. H., Salo, S. A. & Overland, J. E., 1983. Drag measurements for first-year sea ice over a shallow sea, *J. geophys. Res.*, **88**, 2853–2862.

Prik, Z. M., 1959. Mean position of surface pressure and temperature distribution in the Arctic, *Tr. Arkticheskogo Nauchn.-Issled. Inst.*, **217**, 5–24 (in Russian).

Schwerdtfeger, W., 1979. Meteorological aspects of the drift of ice from the Weddell Sea toward the midlatitude westerlies, *J. geophys. Res.*, **84**, 6321–6328.

Smith, S. D., Banke, E. G. & Johannessen, O. M., 1970. Wind stress and turbulence over ice in the Gulf of St. Lawrence, *J. geophys. Res.*, **75**, 2803–2812.

Vinje, T. E., 1982. The drift pattern of sea ice in the Arctic with particular reference to the Atlantic approach, in *The Arctic Ocean*, pp. 83–96. Wiley, New York.